Design and realisation of a microwave three-dimensional imaging system with application to breast-cancer detection

Zhurbenko, Vitaliy; Rubæk, T.; Krozer, V.; Meincke, P.

Published in:
I E T Microwaves Antennas & Propagation

Link to article, DOI:
10.1049/iet-map.2010.0106

Publication date:
2010

Document Version
Peer reviewed version

Design and Realization of a Microwave Three-Dimensional Imaging System with Application to Breast-Cancer Detection

Vitaliy Zhurbenko, Tonny Rubæk, Viktor Krozer, Peter Meincke

Technical University of Denmark, Department of Electrical Engineering, Ørsteds Plads, b. 348, 2800 Kgs. Lyngby, Denmark.

Abstract— This paper describes an active microwave imaging system for noninvasive detection of breast cancer based on dedicated hardware. 32 transceiving channels are used to measure the amplitude and phase of the scattered fields in the three-dimensional (3D) imaging domain using electronic scanning. The 3D inverse electromagnetic scattering problem is then solved in order to reconstruct the distribution of the complex permittivity in the imaging domain. The dedicated hardware is based on an array architecture allowing for a short acquisition time while maintaining a high sensitivity, which is important for measurement accuracy and reproducibility as well as for patient comfort. The dedicated hardware achieves a receiver noise figure of 2.3 dB at a gain of 97 dB. The operating frequency range is from 0.3 GHz to 3 GHz. The image acquisition time at one frequency is approximately 50 seconds and an image is created within 2 hours using the single-frequency reconstruction algorithm. The performance of the system is illustrated by an analysis of the standard deviations in amplitude and phase of a series of measurements as well as by a simple image reconstruction example.

Key words—Microwave imaging, monopole antennas, heterodyne receivers, power dividers, transceiver arrays, ultrawideband components.

I. Introduction

Worldwide, more than a million women are diagnosed with breast cancer every year. It is the most common type of cancer and the second leading cause of cancer-related deaths among women today [1]. Early detection is a key factor to assure efficient treatment of the cancer and to this end, breast-cancer screening is an important tool. This has motivated researchers to improve existing screening methods and to develop alternative or complimentary modalities to the widely used X-ray mammography.

During the last decade, microwave-based systems for detection of breast cancer have gained attention from an

increasing number of research groups [3]-[13] and the modality is currently progressing towards practical use in clinical environments [2]-[4]. The interest in microwave imaging for this purpose is driven not only by the reported differences between the electromagnetic properties of benign and malignant tissue, which allows for detection of tumors [14]-[23], but also by the advances in microwave imaging arrays, component availability, and the rapid increase of computational power for calculation of complex electromagnetic problems [7].

The microwave-imaging techniques for breast-cancer detection can be divided into passive and active techniques. Passive microwave imaging is usually referred to as thermography [24]-[27] and is based on the measurement of the electromagnetic field spontaneously emitted by warm bodies according to Planck's law. In active systems, the sensing is accomplished by irradiating the object to be imaged and measuring the response in terms of the resulting electromagnetic field.

Active microwave imaging modalities can, in turn, be divided into microwave microscopy, hybrid modalities, microwave tomography, and time-domain techniques. The microwave microscope is based on the change in the resonant frequency of a microwave resonator which results from the interaction of the electromagnetic field of the resonator and objects positioned at the end of the resonating cavity, such as breast tumors [28], [29]. Subwavelength resolution has been reported using this technique. Hybrid techniques, like microwave-induced thermal acoustic imaging [30]-[32] and ultrasound-guided microwave imaging [33], use a combination of electromagnetic and acoustic waves to extend the detection range of physiological and pathological conditions of tissues.

In tomographic systems, the object to be investigated is irradiated by a known incident field and the resulting scattered field is measured by a number of receiving antennas. Using this information, the electromagnetic parameters of the object are reconstructed by solving an inverse problem based on Maxwell equations [2], [12], [34]-[37].

Time-domain ultrawideband radar techniques are based on radar principles in which one seeks to determine the location-of-origin of the scattered time-domain signal [8]-[10]. Since measurement accuracy and high dynamic range are key requirements for good image quality, all time-domain microwave imaging methods reported so far rely on swept frequency-domain measurements in combination with inverse Fourier transformation [38]-[45].

Results of clinical use of full-breast imaging have, at the time of writing, been reported for passive systems [25], 2D tomographic systems [45], and radar-based ultra-wideband systems [4].

This paper describes the active microwave 3D imaging system which uses frequency-domain measurements in

conjunction with a multi-channel architecture with individual measurement units and electronic scanning allowing for a short data-acquisition time required for practical use in a clinical setup. The proposed system provides simultaneous multichannel recording. In Section II, the overall concept and system building blocks are described and in Section III, the image reconstruction algorithm is briefly outlined. The performance of the system is investigated in Section IV.

II. Design of the Microwave Imaging System

The purpose of the hardware is to generate an incident field to irradiate the target, i.e., the breast, and measure the resulting scattered field. A schematic block-diagram and the principle of operation are illustrated in Fig. 1. The

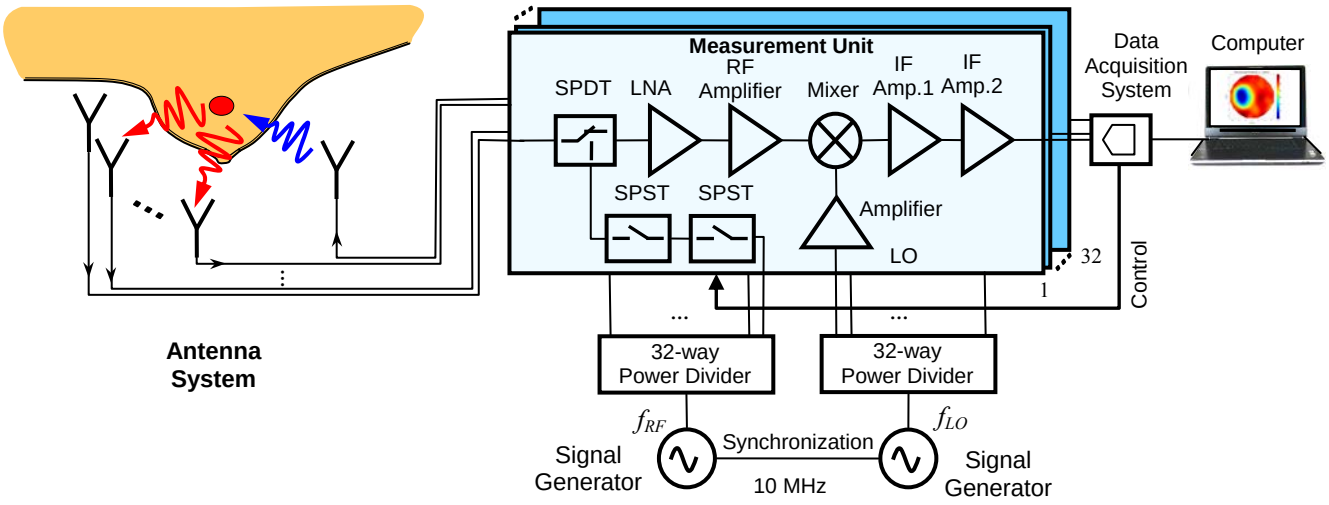

Fig. 1. The microwave imaging system architecture. The individual measurement unit consists of a low-noise amplifier (LNA), RF amplifiers, a passive mixer, a two-stage intermediate frequency amplifier (IF Amp.1, and IF Amp.2), a single-pole double-throw (SPDT), and two single pole single throw (SPST) switches.

microwave imaging system contains 32 measurement channels and is designed to operate in the frequency range up to 3 GHz. It consists of an antenna system connected to measurement units, RF signal sources, and a data acquisition system connected to a computer. The system also employs broadband power dividers for the distribution of the RF signal to the 32 measurement channels.

The choice of 32 channels is based on a trade-off between maximizing the amount of measurements available for the imaging algorithm and the limited space which is available for the measurement units and antennas in the imaging system.

The system applies individual measurement units for each channel, i.e., each antenna. Each channel can operate in either transmit or receive mode, allowing for feeding one transmitting antenna at a time and measuring the field at the remaining 31 antennas, resulting in a total of 992 measurements of phase and amplitude. Due to the reciprocity of the system, half of these measurements are redundant, but including them in the inversion reduces the impact of noise in the measurements.

The channel topology is based on superheterodyne principles, which is an attractive architecture in highly sensitive instrumentation receivers. The configuration can extend the dynamic range considerably compared to the more commonly used combination of a two-port network analyzer connected to a switching network [4], [39] with the dynamic range of the superheterodyne imaging system reported in [3] exceeding 120 dB. The multi-channel architecture also allows for a fast data acquisition, since the measurements are performed simultaneously for all receiving channels. All 32 measurement units are identical and their mode of operation (transmit or receive) is controlled by digital outputs of the data acquisition system connected to the switches in the measurement units. The acquisition time for one system state (one antenna transmitting, 31 receiving) is approximately 1.5 second using 10 000 samples per channel. The choice of samples per channel is a trade-off between the measurement speed and the noise floor of the system since fewer samples per channel reduces the measurement time but also increases the effective noise floor of the system. The overall acquisition time for all states necessary to create a 3D image, i.e., all 32 antennas, in turn, acting as transmitters, is approximately 50 seconds, including the necessary switching time for the solid-state SPDT switches as well as time needed for storing the measured data on the computer.

The incident field is generated by a signal generator operating at the frequency f_{RF} connected to the antenna system through a power divider and the switches in the measurement unit. The maximum power available at the terminal of the antennas depends on the power available from the generator and equals -5 dBm in the current system. However, this power level could be increased to further extend the dynamic range.

The field transmitted by the antenna illuminates the object (i.e, the breast) which is located in a measurement tank. The resulting field is collected by the remaining 31 antennas and the output of each of the receiving antennas is amplified and down-converted to f_{IF} by the individual measurement units. The LO signal generator provides a signal with frequency $f_{RF} + f_{IF}$, which is used to drive a down-converter.

The isolation between the Tx-path and the Rx-path in the individual measurement units when operating in transmitting mode is not perfect. As a consequence, a finite amount of feedthrough reaches the mixer and produces

an IF component at the output of the measurement unit. This leakage effect arises mainly from the -40 dB coupling of the transmitted power through the SPDT switch in off mode and is used as reference to obtain coherent measurements of the scattered field.

The measurement units are connected to a data acquisition system comprised of a lowpass anti-aliasing filter and an analog-to-digital converter which records the amplitude and phase of the incoming harmonic signal. These are then stored for later use in the reconstruction algorithm.

The measurement units are designed to be lightweight and compact. This allows for them to be attached directly to the antenna array, as can be seen in the photograph of the system in Fig. 2.

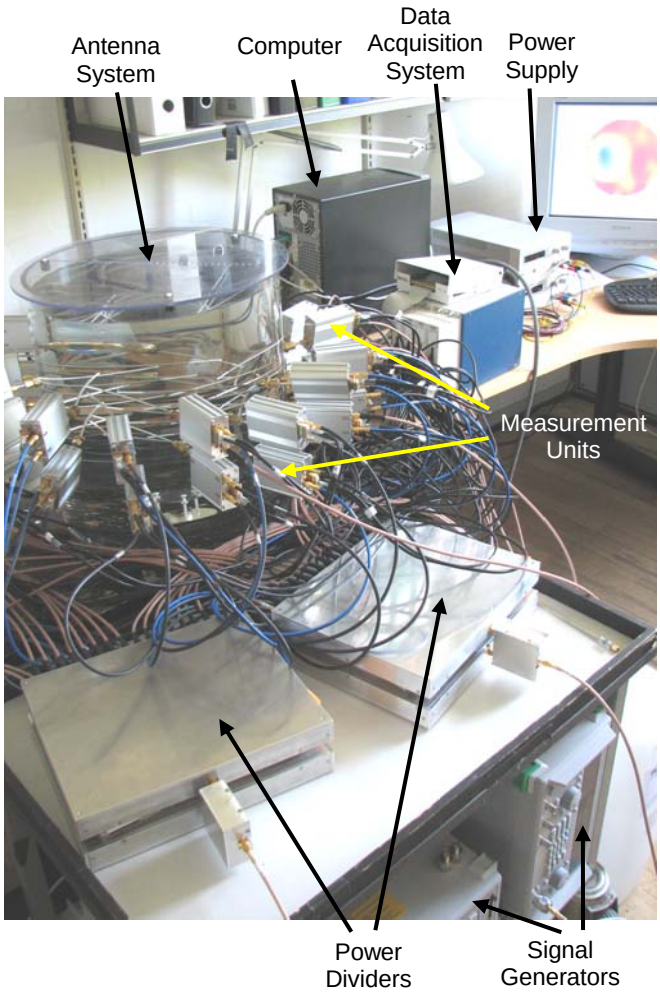

Fig. 2. Photograph of the 3D microwave imaging system.

Such a realization eliminates interconnecting cables between the antennas and the measurement modules, which would introduce extra noise in the receiving path and contribute to the parasitic coupling between the channels.

A. Antenna system

The 32 antennas used in the system are of simple monopole type, introduced for microwave imaging in [35] and employed for ultrasound-guided breast imaging in [33]. The individual antenna consists of a 3.58 mm diameter coaxial cable (Micro Coax UT141-SS [47]) from which the outermost 3.5 cm of the outer conductor has been stripped, exposing the dielectric, as depicted in Fig. 3 (b). The antennas are positioned in a cylindrical array, shown in the schematic diagram and photograph in Fig. 4, inside a measurement tank. This tank is filled with a glycerin-water coupling liquid which mimics the electromagnetic parameters of the breast [22], thereby assuring that a maximum of the transmitted field is coupled to the interior of the breast. Since the liquid is lossy, the reflected signals from the side of the measurement tank are attenuated, implying that the antenna system is not influenced by these reflections or by scattering objects outside the measurement tank. The losses in the liquid, and to some extent in the breast, also explain the need for the large dynamic range of the measurement units in spite of the antennas being positioned relatively close to each another. The simplicity of the antennas implies that they are inexpensive and easy to manufacture and the small size allows for positioning many antennas close to the imaging domain. The operating frequency band of the employed antenna is extended when inserted in the lossy coupling liquid, as can be seen from the measurements in Fig. 3(a). This allows for a return loss of more than 5 dB at frequencies above 0.5 GHz. The main resonance of the antenna is seen to be at approximately 900 MHz.

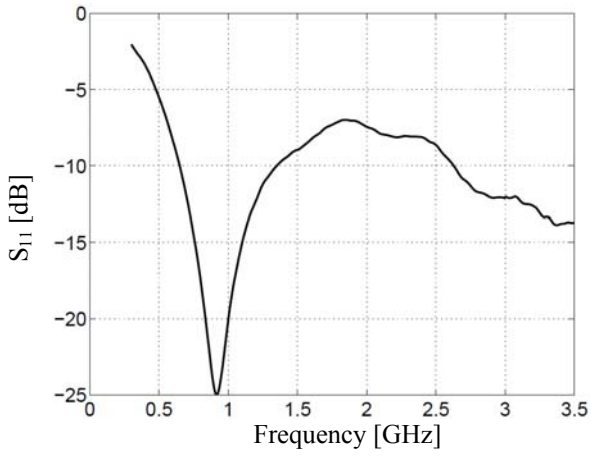

(a)

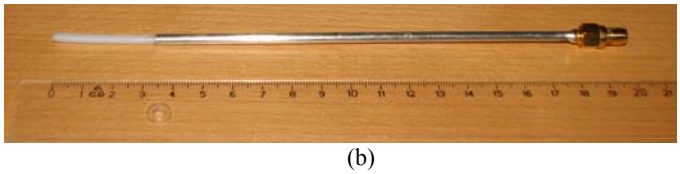

(b)

Fig. 3. The antenna element. (a) The measured scattering parameter S_{21} of the antenna immersed in an 80 % - 20 % glycerin-water solution. (b) Photo.

During examination, the patient is to lie prone on an examination table above the measurement tank with one breast suspended through an aperture positioned above the center of the antenna array. The imaging domain, in which the breast is assumed to be fully enclosed, is then introduced as a hemispherical region immediately below this aperture.

To ensure that the antennas cover the entire imaging domain, the 32 antennas are positioned in a cylindrical array with a radius of 8 cm are used as shown in Fig. 4.

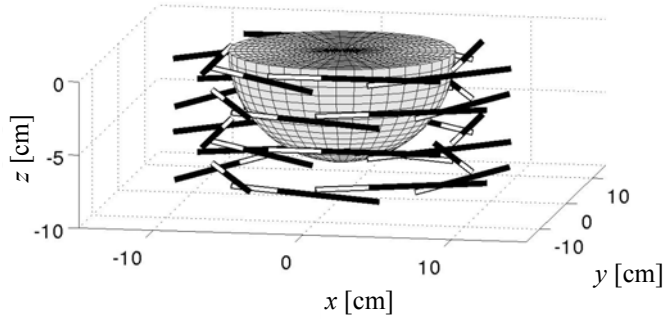

(a)

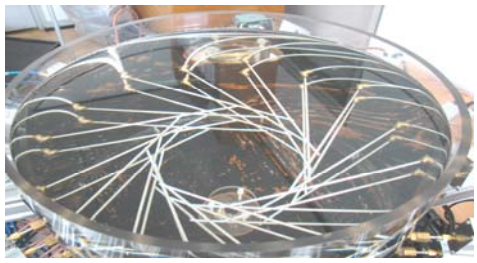

(b)

Fig. 4. Antenna system. (a) Schematic drawing showing antenna array and imaging domain. (b) Photograph showing antenna array.

The antennas are oriented horizontally and positioned in 4 rows with 8 antennas in each row. In Fig. 4 (a), the exposed dielectric of the antennas is illustrated by the white lines and the coaxial cables are indicated by the black lines. The antennas are held in place by the coaxial cables.

In addition to being small, easy and cheap to manufacture, the monopole antennas have the advantage of being computationally inexpensive to include in the method of moments model used in the reconstruction algorithm (described in Section III) to solve the forward problem. This eliminates the need to use simplified models of the antennas, e.g., Hertzian dipoles, thereby improving the performance of the algorithm.

B. Measurement units

The wide operating frequency band establishes demanding requirements for the circuit blocks in the receiver component chain. The measurement units were developed specifically to maximize sensitivity in a wide frequency range and consist of a low-noise amplifier, an RF amplifier, a double-balanced passive mixer, a two-stage IF amplifier, a single-pole double-throw switch, and two single-pole single-throw switches, as shown in Fig.1.

In the individual units, the signal received by the antenna is first routed through an SPDT switch. This switch is used to enable time-division diplexing between the transmit mode and the receive mode. Before feeding the received signal into the down-converting mixer it is amplified with an LNA and an RF amplifier. The LNA is a gallium arsenide amplifier chip with external input and output matching circuits. This LNA is a key component of the high-sensitive measurement units, and is based on an ultra low-noise amplifier (CGY2108 from OMMIC [48]), which has a typical noise figure of 0.5 dB. Wideband input and output matching circuits have been designed in order to extend the operating frequency band of the LNA at the expense of a degradation in noise figure. As a result, the LNA has a noise figure of 1.2 dB, and an associated gain of 25 dB at midband.

The following RF amplifier (Hittite HMC478 [49]) provides a gain and a noise figure of 22 dB and 2.5 dB, respectively, and is used to improve the overall sensitivity of the receiver.

The passive mixer improves the receiver linearity. The mixer (Mini-Circuits ADE-30W [50]) down-converts the input signal to the IF band where it receives further amplification and filtering. The diode-based mixer requires no bias and has a conversion loss of typically 8 - 9 dB at the considered frequencies. The mixer output signal from the IF port is amplified using a two-stage IF amplifier (Analog Devices AD822 [51]) with a total gain of 59 dB.

The LO signal is routed to the mixer through a network consisting of broadband power dividers and an amplifier, the latter of which is used to compensate for the losses caused by the power division.

The measurement units provide a total gain of 97 dB with a 2.3 dB noise figure at midband in the receiving path. The noise floor was measured to be below –140 dBm over a 1 kHz bandwidth centered at the IF frequency 1 kHz.

In transmit mode, a harmonic RF signal is fed into the antenna from the signal generator and power divider and is multiplexed through the SPDT (M/A-COM MASW-007071 [52]) and the SPST (M/A-COM MASW-007071 [53]) switches. Two cascaded SPST switches are implemented in order to achieve high isolation when the units are operating in receiving mode. The isolation between the channels of the imaging system is approximately 120 dB for antennas mounted next to each other, and, as expected, better isolation is achieved for antennas mounted on opposite

sides of the imaging domain. This value was measured at 900 MHz and it decreases with increasing frequency. Since the received field is much stronger (in excess of 50 dB) at the antennas adjacent to the transmitter, the limiting factor in terms of isolation is the isolation between the channels mounted on opposite side of the imaging system.

The measurement units are powered by a ± 5 V supply. A view of a unit with the top cover and shielding fences removed is shown in Fig. 5.

It was built on Rogers RO4003 substrate and the backside of the module (not shown) is used for the bias circuit distribution. Careful routing on the printed circuit board, especially for the control and biasing signals, guarantees oscillation- and cross-talk free operation, which are otherwise major issues for this type of system. The overall size of the module, without the RF connectors, is 80 mm × 63.5 mm × 30 mm.

C. Signal sources and power dividers

Two signal sources provide the frequency reference for the LO and the incident wave generation within the system. The sources drive all 32 measurement units through the 32 port power divider as indicated in Fig. 1. In the current configuration, the signal sources are based on two synchronized commercially available generators (Agilent N5181A-506, [54]).

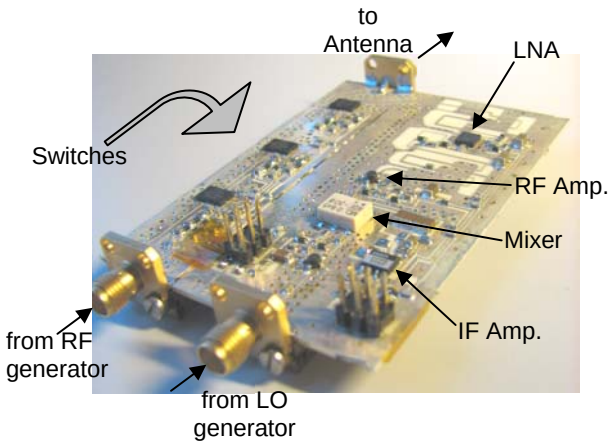

Fig. 5. Photograph of the measurement unit with shielding fences removed. The block diagram of the unit is shown in Fig. 1.

The 32-way power dividers are identical and consist of one 2-way and two 16-way broadband Wilkinson power dividers (also known as “in-line” power dividers [55]) connected in series. The 16-way power divider network is a 4-level tree three-step Wilkinson divider and is realized on a large single substrate (0.8 mm thick) as shown in Fig.6. The shape of the quarter-wave transmission lines resembles a meander line and this shape has been chosen as a tradeoff between overall size of the structure, and parasitic electromagnetic coupling between the circuit elements. Optimum performance would have been obtained with the circuit elements completely decoupled but the system-

cost requirements demand a more tightly-packed configuration.

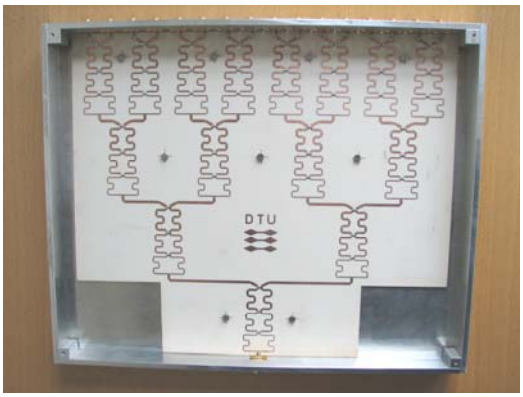

Fig. 6. 16-port wideband power divider with meander shaped quarter-wave lines.

D. Data acquisition

The down-converted signal is digitized by a 32 channel 18 Bit analog-to-digital converter. The data is transferred via the Peripheral Component Interconnect interface to a computer where the signal processing is accomplished using LabVIEW software. The digitized IF signal is filtered using a 5th order bandpass filter.

III. Image Reconstruction Method

To reconstruct the distribution of the constitutive electromagnetic parameters, i.e., permittivity and conductivity, of the breast, a hemispherical imaging domain is introduced in the center of the antenna setup. This domain is indicated by the hemisphere in Fig. 4(a) and is divided into cubic cells. In each of these cells, the constitutive parameters are assumed to be constant and are represented by their squared complex wave numbers

$$k^2(\mathbf{r}) = \omega^2 \mu_0 \varepsilon(\mathbf{r}) + i\omega\mu_0 \sigma(\mathbf{r}). \tag{1}$$

In this expression, ω is the angular frequency, μ_0 is the free-space permeability, the use of which indicates that the imaging domain is assumed nonmagnetic, and the permittivity and conductivity are given by ε and σ, respectively. The imaginary unit is given by i, $\mathbf{r}$ is a position vector, and the time notation $e^{-i\omega t}$ has been applied.

The image-reconstruction algorithm used in the microwave imaging system is based on nonlinear inverse scattering in which the distribution of the constitutive electromagnetic parameters permittivity and conductivity is determined by solving the minimization problem

$$\begin{aligned}\underline{k}^2 &= \arg\min\left\{\left\|\underline{S}^{\text{meas}} - \underline{S}^{\text{calc}}\left(\underline{k}^2\right)\right\|_2^2\right\} \\ &= \arg\min\left\{\left\|\underline{S}^{\text{res}}\left(\underline{k}^2\right)\right\|_2^2\right\}\end{aligned} . \tag{2}$$

In this expression, the vector $\underline{k}^2$ holds the squared complex wave numbers of the individual cells of the imaging domain while the vector $\underline{S}^{\text{meas}}$ holds the measured signals, and $\underline{S}^{\text{calc}}(\underline{k}^2)$ holds the calculated signals for the distribution of squared complex wave numbers given by the vector $\underline{k}^2$. The vector $\underline{S}^{\text{res}}(\underline{k}^2)$ is the residual vector.

The so-called log-amplitude unwrapped phase formulation of the measured and calculated signals, first introduced for microwave imaging in [56], is used in the reconstruction algorithm. This implies that each measured and calculated signal is represented by two elements in the vectors $\underline{S}^{\text{meas}}$ and $\underline{S}^{\text{calc}}$. These elements are given by the difference in the logarithm of the amplitudes of the signals (measured or calculated) obtained with an empty system and the corresponding signals with the breast inserted in the system and the corresponding unwrapped difference in phase, respectively. The benefits of using this formulation as well as details on how to unwrap the phases are given in [56], [57].

The minimization problem is solved using a Newton algorithm, similar to the one described in [58], in which the following three steps are performed in each of the N Newton iterations:

1. Calculate the elements of the vector $\underline{S}_n^{\text{res}}$ and the corresponding Jacobian matrix for the distribution of squared complex wave numbers $\underline{k}_n^2$ using a method of moments code [59], [60].

2. Determine the update vector $\underline{\Delta k}_n^2$ by solving the linear inverse problem

$$\underline{\Delta k}_n^2 = \arg\min\left\{\left\|\underline{\underline{J}}_n \underline{\Delta k}_n^2 - \underline{S}_n^{\text{res}}\right\|_2^2\right\} \quad \text{subj. to regularization.} \tag{3}$$

Here $\underline{\underline{J}}_n$ is the Jacobian matrix and the regularization is obtained by use of the iterative conjugated gradient least squares algorithm [61, Sec. 6.3] and to obtain the best overall performance of the reconstruction algorithm, an over-regularized solution is used, i.e., a solution obtained using few conjugate gradient least squares algorithm iterations [58]. In the present setup, 4 iterations with the conjugate gradient least squares algorithm are used.

3. Update the values of $\underline{k}_n^2$ using

$$\underline{k}_{n+1}^2 = \underline{k}_n^2 + \alpha_n \underline{\Delta k}_n^2 \tag{4}$$

with α_n being the Newton step. The primary reason for using the Newton step is to allow for an easy unwrapping of the phase of the calculated signals as described in [56], [58].

The reconstruction algorithm typically finishes after 8 to 12 Newton iterations, with each Newton iteration taking just over ten minutes to complete. Hence, the total reconstruction time is between 90 and 130 minutes.

IV. Performance

An essential aspect of this system is the calibration routine. The electromagnetic field in an empty chamber is used as a reference for the scattered field from an object. Thus, the imaging procedure consists of a scan of the object (breast) followed by a scan of the empty system. This implies that the performance of the system to a large extent depends on repeatability of the measurement results.

In order to estimate the precision of the system, the amplitude and phase variations of the measured signals in $\underline{S}^{meas}$ have been observed for a number of measurements and their distributions analyzed. To this end, 1000 measurements, performed with an interval of 1 second, with a single transmitter, a single receiver, and an empty system were acquired. The amplitude and phase variations for this measurement series are shown in Fig. 7 with the bars indicating the actual observed frequencies (number of observed incidents) while the crosses indicate the expected frequencies obtained from fitting a normal distribution to the measured data. The values in Fig. 7(a) are given as the normalized deviation from the mean value of the amplitude. The presented results are for the midband measurements using transmitted power level of -35 dBm. The data is approximately normally distributed as illustrated by the relatively good fit of the data to the best-fit normal distribution. The observed standard deviation of the best-fit normal distribution of the phase and normalized amplitude are 0.36 ° and 0.31 %, respectively.

In addition to these uncertainties a slow change in signal amplitude and phase has been observed in the imaging system when doing prolonged measurements, i.e., measurements over several hours or even days. This drift is mainly due to ambient temperature variations but is not an issue in the measurement series presented here which had a measurement time of less than an hour.

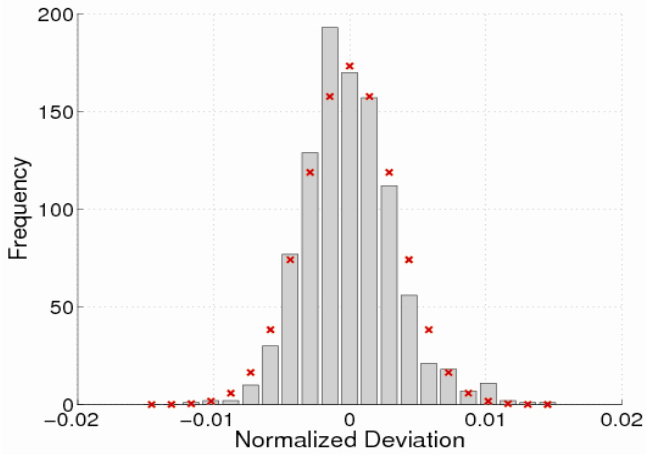

(a)

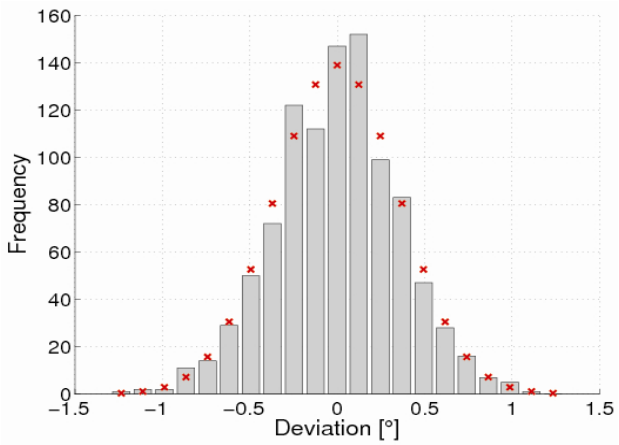

(b)

Fig. 7. Investigation of the system precision. (a) Amplitude measurements. (b) Phase measurements. The bars indicate the observed frequencies while the crosses indicates the best-fit normal distributions. In both figures, the values are given as the deviation from the mean measured values.

In order to demonstrate the performance of the microwave imaging system, a reconstruction of a simple cylindrical object was chosen as a first scenario. The results reported here are for a single frequency reconstruction at 900 MHz - the main resonance of the antenna system. The measured return loss of the antennas at this frequency is approximately 25 dB. A side length of 5 mm has been chosen for the cubic cells of the imaging domain. The size of these cells is a trade-off between reconstruction time and spatial resolution, with more and smaller cells increasing the reconstruction time. When choosing the cell size, the wavelength in the coupling liquid should also be considered. In the example presented here, the coupling liquid has a relative permittivity of 31.5 and the wavelength at 900 MHz is thus 5.9 cm. The 5 mm side length of the cells thus corresponds to 0.084 wavelengths, indicating that the resolution is more likely limited by the frequency than the cell size.

The object positioning and microwave images are shown in Fig. 8. The images were formed using the reconstruction algorithm described in III after 6 Newton iterations. The object was a Teflon cylinder of 20 mm radius and 40 mm height. The relative permittivity of the cylinder was 2.1 and the conductivity was essentially zero. The object was shifted from the center of the imaging domain by 3 cm in the negative *y* direction. The relative permittivity and conductivity of the coupling liquid (water – glycerin solution in 20 % - 80% proportion measured with an Agilent dielectric probe kit 85070 E) were 31.5 and 1.05 S/m, respectively. The images represent the spatial distribution of relative permittivity (Fig. 8(b)) and conductivity (Fig. 8(c)) in the imaging domain with the object visible in both images. However, the image for relative permittivity (Fig. 8(b)) reflects the geometrical shape and size of the object better than the conductivity image. The position is also unambiguously identified from the images, though the actual value of the complex permittivity of the object is not perfectly reconstructed. The increased level of the artifacts in the conductivity image compared to the permittivity image has been observed for a number of different imaging tests with the system, both on measured and simulated data. It has also been observed in a number of different imaging systems using similar imaging technique [2], [3], [5], [6]. A scaling of the real and imaginary parts of the complex wavenumbers has been proposed to remedy this [2], but in the system presented here, we have found that although this approach can improve the conductivity images in some cases, it is just as likely to deteriorate the quality of the permittivity images. Hence, such a scaling has not been applied in the test images presented here.

It should be noted that the imaging experiments described in this section are for demonstration purposes only, and the images are shown without any kind of image post processing, filtering or imaging algorithm adjustments. There was no *a priori* information taken into consideration, except for the dielectric properties of the coupling medium, which have been measured prior to the image acquisition.

In the next experiment, two smaller spherical objects have been imaged. The objects were 1 cm radius plastic balls filled with water ($\varepsilon_r = 79$, $\sigma = 0.55$ S/m). This imaging scenario is closer to reality since the permittivity of malignant breast tissue is usually very high due to the high water and blood content. The reconstructed images at 1.5 GHz are shown in Fig. 9. The relative permittivity and conductivity of the coupling liquid at 1.5 GHz (water – glycerin solution in 10 % - 90% proportion) were 12 and 0.86 S/m, respectively.

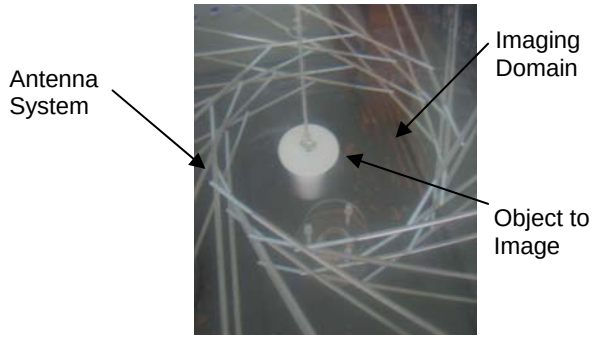

(a)

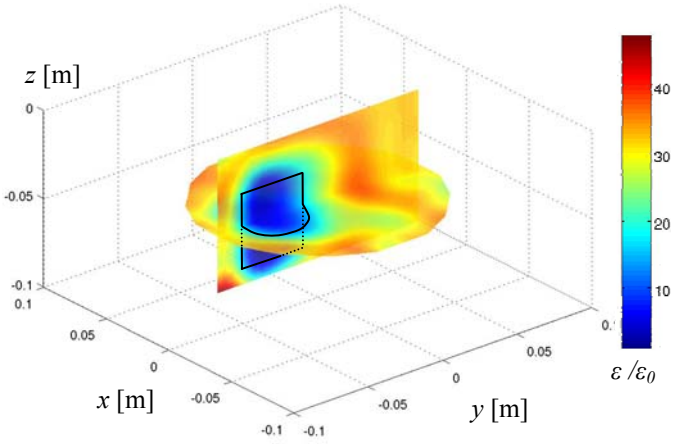

(b)

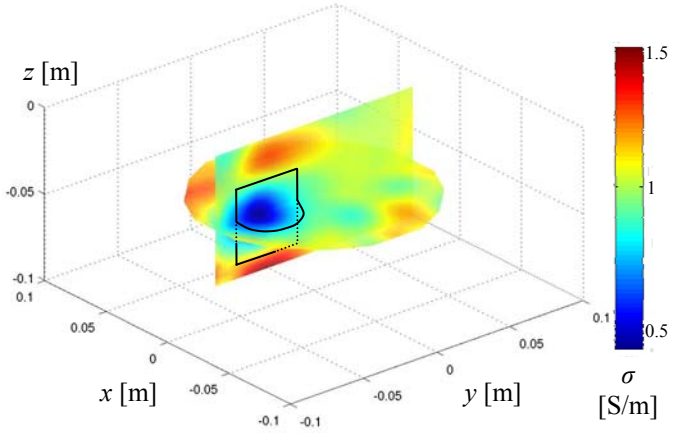

(c)

Fig. 8. Three-dimensional imaging of a cylindrical object. (a) Photograph of the imaging domain. Reconstructed distribution of (b) relative permittivity and (c) conductivity. The black line marks the contour of the object to image.

As in the previous case, the targets are visible in both images. The position is also detected from the images, though the actual value of the complex permittivity of the object is not perfectly reconstructed. It is also interesting to notice that this imaging experiment demonstrates subwavelength imaging properties of the system.

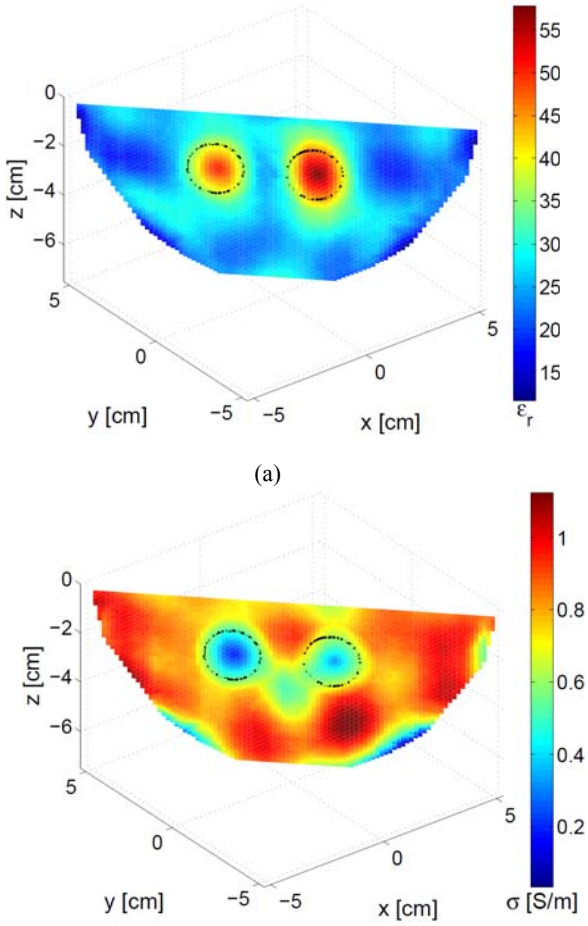

Fig. 9. 2D slice through the detected target location. Reconstructed distribution of (a) relative permittivity and (b) conductivity. The black line marks the contour of the object to image.

The wavelength in the coupling medium is approximately 5.8 cm. Near-field measurements with the current system allowed visualization of targets which are smaller than the wavelength.

V. Conclusion

An experimental prototype of a 3D microwave imaging system has been presented. A multichannel architecture, capable of measuring the vector electric field distribution inside of the imaging domain, has been implemented in order to reduce total scanning time of the system, yielding a data acquisition time of approximately 50 seconds. The hardware operates in the frequency range from 0.3 GHz to 3 GHz and is capable of measuring low level signals above the -140 dBm system's noise floor. The dynamic range of the system is limited by the channel to channel isolation but also depends on the available transmitting power.

3D images of the dielectric properties of the test objects have been obtained. The images can be generated in around 100 minutes using the single frequency reconstruction algorithm. A reasonable agreement in the shape and position of the object is obtained.

While the objects are visible in both property images, there is still room for improvement. Further image improvement is likely possible by adjusting the parameters of the single-frequency reconstruction algorithm or by applying a multiple-frequency reconstruction algorithm.

REFERENCES

[1] American Cancer Society, Inc., American Cancer Society Web Page, Available online: http://www.cancer.org/, April 2007.

[2] K. D. Paulsen, P. M. Meaney, and L. C. Gilman, Alternative Breast Imaging. Four Model-Based Approaches, Boston: Springer Science + Business Media, Inc., 2005.

[3] P. M. Meaney, M. W. Fanning, D. Li, S. P. Poplack, and, K. D. Paulsen" A Clinical Prototype for Active Microwave Imaging of the Breast," IEEE Transactions On Microwave Theory And Techniques, vol. 48, no. 11, pp. 1841–1853, November 2000.

[4] M. Klemm, I. Craddock, J. Leendertz, A. Preece, and R. Benjamin, "Experimental and Clinical Results of Breast Cancer Detection Using UWB Microwave Radar," IEEE AP-S International Symposium, 2008.

[5] S. Y. Semenov, A. E. Bulyshev, A. Abubakar, V. G. Posukh, Y. E. Sizov, A. E. Souvorov, P. M. van den Berg, and T. C. Williams, "Microwave-Tomographic Imaging of the High Dielectric-Contrast Objects Using Different Image-Reconstruction Approaches," IEEE Transactions on Microwave Theory and Techniques, vol. 53, no. 7, pp. 2284–2294, July 2005.

[6] C. Yu, M. Yuan, J. Stang, E. Bresslour, R. T. George, G. A. Ybarra, W. T. Joines, Q. H. Liu, "Active Microwave Imaging II: 3-D System Prototype and Image Reconstruction from Experimental Data," IEEE Transactions on Microwave Theory and Techniques, vol. 56, no. 4, pp. 991-1000, 2008.

[7] E. C. Fear, S. C. Hagness, P. M. Meaney, M. Okoniewski, and M. A. Stuchly, "Enhancing Breast Tumor Detection with Near-Field Imaging," IEEE Microwave Magazine, vol. 3, issue 1, pp. 48–56, March 2002.

[8] E. C. Fear, and M. A. Stuchly," Microwave Detection of Breast Cancer," IEEE Transactions on Microwave Theory and Techniques, vol. 48, no. 11, pp. 1854-1863, 2008.

[9] Y. Xie, B. Guo, J. Li, and P, Stoica, "Novel Multistatic Adaptive Microwave Imaging Methods for Early Breast Cancer Detection", Journal on Applied Signal Processing, vol. 2006, pp. 1-12, 2006.

[10] P. Kosmas and C. M. Rappaport, "Time Reversal with the FDTD Method for Microwave Breast Cancer Detection," IEEE Transactions on Microwave Theory and Techniques, vol. 53, no. 7, pp. 2317–2323, July 2005.

[11] M. Elsdon, D. Smith, M. Leach, and S. J. Foti, "Experimental Investigation of Breast Tumor Imaging Using Indirect Microwave Holography," Microwave and Optical Technology Letters, vol. 48, no. 3, pp. 480–482, March 2006.

[12] A. Fhager, P. Hashemzadeh, M. Persson, "Reconstruction Quality and Spectral Content of an Electromagnetic Time-Domain Inversion Algorithm," IEEE Transactions on Biomedical Engineering, vol. 53, no. 8, pp. 1594-1604, August 2006.

[13] T. Rubaek, V. Zhurbenko, "Prototype of Microwave Imaging System for Breast-cancer Screening," 13th International Symposium on Antenna Technology and Applied Electromagnetics and the Canadian Radio Science Meeting, ANTEM/URSI 2009, pp. 1-4, 15-18 February 2009.

[14] U. Khan, N. Al-Moayed, N. Nguyen, M. Obol, K. Korolev, M. Afsar, S. Naber, ”High Frequency Dielectric Characteristics of Tumorous and Nontumorous Breast Tissues,” IEEE MTT-S International Microwave Symposium Digest, pp. 1341-1344, 2007.

[15] M. Stuchly and S. Stuchly, “Dielectric Properties of Biological Substances – Tabulated,” Journal of Microwave Power, vol. 15, no. 1, pp. 19–26, 1980.

[16] K. Foster and H. Schwan, “Dielectric Properties of Tissues and Biological Materials: A Critical Review,” CRC Critical Reviews in Biomedical Engineering, vol. 17, no. 1, pp. 25–104, 1989.

[17] L. Sha, E. Ward, and B. Stroy, “A Review of Dielectric Properties of Normal and Malignant Breast Tissue,” Proceedings of the IEEE SoutheastCon, 2002, pp. 457–62, 2002.

[18] W. T. Joines, Y. Zhang, C. Li, and R. L. Jirtle, “The Measured Electrical Properties of Normal and Malignant Human Tissues From 50 to 900 MHz,” Medical Physics, vol. 21, no. 4, pp. 547–50, 1994.

[19] M. Lazebnik, L. McCartney, D. Popovic, C. B. Watkins, M. J. Lindstrom, J. Harter, S. Sewall, A. Magliocco, J. H. Booske, M. Okoniewski, and S. C. Hagness, “A Large-Scale Study of the Ultrawideband Microwave Dielectric Properties of Normal Breast Tissue Obtained From Reduction Surgeries,” Physics in Medicine and Biology, vol. 52, no. 10, pp. 2637–2656, 2007.

[20] M. Lazebnik, D. Popovic, L. McCartney, C. B. Watkins, M. J. Lindstrom, J. Harter, S. Sewall, T. Ogilvie, A. Magliocco, T. M. Breslin, W. Temple, D. Mew, J. H. Booske, M. Okoniewski, and S. C. Hagness, “A Large-Scale Study of The Ultrawideband Microwave Dielectric Properties of Normal, Benign and Malignant Breast Tissues Obtained From Cancer Surgeries,” Physics in Medicine and Biology, vol. 52, no. 20, pp. 6093–6115, 2007.

[21] S. Poplack, K. Paulsen, A. Hartov, P. Meaney, B. Pogue, T. Tosteson, M. Grove, S. Soho, and W. Wells, “Electromagnetic Breast Imaging: Average Tissue Property Values in Women With Negative Clinical Findings,” Radiology, vol. 231, no. 2, pp. 571–580, 2004.

[22] P. Meaney, M. Fanning, T. Raynolds, C. Fox, Q. Fang, C. Kogel, S. Poplack, and K. Paulsen, “Initial Clinical Experience with Microwave Breast Imaging in Women with Normal Mammography,” Academic Radiology, vol. 14, no. 2, pp. 207–218, 2007.

[23] W. Hurt, J. Ziriax, and P. Mason, “Variability in EMF Permittivity Values: Implications for SAR Calculations,” IEEE Transactions on Biomedical Engineering, vol. 47, no. 3, pp. 396–401, 2000.

[24] R. Tipa and O. Baltag, “Microwave Thermography for Cancer Detection,” Rom. Journ. Phys., vol. 51, Nos. 3–4, pp. 371-377, 2006.

[25] V. P. Zharov et al., ”Combined Interstitial Laser Therapy for Cancer Using Microwave Radiometric Sensor and RODEO MRI Feedback. 1. Microwave radiometry,” Proceedings of SPIE, vol. 4257, pp. 370–376, July 2001.

[26] K. L. Carr, P. Cevasco, P. Dunlea and, J. Shaeffer ”Radiometric Sensing: An Adjuvant to Mammography to Determine Breast Biopsy,” IEEE MTT-S Int. Microwave Symp. Dig., vol. 2, pp. 929–932, 2007.

[27] B. Stec, A. Dobrowolski, and W. Susek, “Estimation of Deep − seated Profile of Temperature Distribution Inside Biological Tissues by Means of Multifrequency Microwave Thermograph,” IEEE MTT-S Int. Microwave Symp. Dig., vol. 3, pp. 2261-2264, 2002.

[28] O. M. Ramahi, and M. H. Kermani, “Transmission Line Resonators for Breast Tumor Detection,” Antennas and Propagation Soc. Int. Symp., vol. 3A, pp. 803–806, 2005.

[29] X. Wu and O. M. Romahi, “Near-field Scanning Microwave Microscopy for Detection of Subsurface Biological Anomalies,” Antennas and Propagation Soc. Int. Symp., vol. 3, pp. 2444-2447, 2004.

[30] R.A. Kruger, W.L. Kiser, Jr., K.D. Miller, H.E. Reynolds, “Thermoacoustic CT,” IEEE MTT-S Int. Microwave Symp. Dig., vol. 2, pp. 933-936, 2000.

[31] B. Guo, J. Li, H. Zmuda, and M. Sheplak, “Multifrequency Microwave-Induced Thermal Acoustic Imaging for Breast Cancer Detection,” IEEE Transactions On Biomedical Engineering, vol. 54, no. 11, pp. 2000–2010, November 2007.

[32] G. Ku and L. V. Wanga, “Scanning Microwave-Induced Thermoacoustic Tomography: Signal, Resolution, and Contrast,” Medical Physics, vol. 28, issue 1, pp. 4–10, January 2001.

[33] H. Jiang, C. Li, D. Pearlstone, and L. L. Fajardo “Ultrasound-Guided Microwave Imaging of Breast Cancer: Tissue Phantom and Pilot Clinical Experiments,” Med. Phys., vol. 32, no. 8, pp. 2528-2535, August 2005.

[34] S. Y. Semenov, R. H. Svenson, A. E. Bulyshev, A. E. Souvorov, A. G. Nazarov, Y. E. Sizov, V. G. Posukh, A. Pavlovsky, P. N. Repin, A. N. Starostin, B. A. Voinov, M. Taran, G. P. Tatsis, and V. Y. Baranov, ”Three-Dimensional Microwave Tomography: Initial Experimental Imaging of Animals,” IEEE Transactions On Biomedical Engineering, vol. 49, no. 1, pp. 55–63, January 2002.

[35] P. M. Meaney, K. D. Paulsen, A. Hartov, and R. K. Crane, “An Active Microwave Imaging System for Reconstruction of 2-D Electrical Property Distributions,” IEEE Transactions on Biomedical Engineering, vol. 42, no. 10, pp. 1017–1026, 1995.

[36] G. Bindu, V. Thomas, A. Lonappan, A. V. Praveen Kumar, V. Hamsakkutty, C. K. Aanandan, and K. T. Mathew, “Two-Dimensional Microwave Tomographic Imaging of Low-Water-Content Tissues,” Microwave and Optical Technology Letters, vol. 46, no. 6, pp. 599–601, September 2005.

[37] T. Gunnarsson, N. Joachimowicz, A. Diet, C. Conessa, D. Aberg, and J. C. Bolomey “Quantitative Imaging Using a 2.45 GHz Planar Camera,” 5th World Congress on Industrial Process Tomography, Bergen, Norway, September, 2007.

[38] R.Nilavalan, I. J. Craddock, A. Preece, J.Leendertz, and R.Benjamin, ”Breast Cancer Tumour Detection Using Microwave Radar Techniques,” URSI 2004 International Symposium on Electromagnetic Theory, vol. 1, pp. 117–119, 2004.

[39] I. J. Craddock, M. Klemm, A. Preece, J. Leendertz, and R. Benjamin, ”Evaluation of a Hemi-Spherical Wideband Antenna Array For Breast Cancer Imaging,” Electromagnetic Theory Symposium, Ottawa, Canada, 2007.

[40] M. L. Trumbo, B. R. Jean, and R. J. Marks, “A New Modality for Microwave Tomographic Imaging: Transit Time Tomography,” http://web.ecs.baylor.edu/faculty/marks/ REPRINTS/short/3T.pdf.

[41] W. C. Khor, M. E. Bialkowski, A. Abbosh, N. Seman, and S. Crozier, ” An Ultra Wideband Microwave Imaging System for Breast Cancer Detection,” IEICE Trans. Commun., vol. E90-B, no. 9, pp. 2376–2381, September 2007.

[42] H. Wang, M. E. Bialkowski, F. Liu and S. Crozier, “FDTD Investigations into UWB Radar Technique of Breast Tumor Detection and Location,” Auswireless 2006 Conference Papers.

[43] X. Li, S. C. Hagness, B. D. Van Veen, and D. van der Weide, “Experimental Investigation of Microwave Imaging via Space-Time Beamforming for Breast Cancer Detection,” IEEE MTT-S Int. Microwave Symp. Dig., vol. 1, pp. 379–382, 2003.

[44] X. Li, S. K. Davis, S. C. Hagness, D. W. van der Weide, and B. D. Van Veen, “Microwave Imaging via Space–Time Beamforming: Experimental Investigation of Tumor Detection in Multilayer Breast Phantoms,” IEEE Transactions On Microwave Theory And Techniques, vol. 52, no. 8, pp. 1856–1865, August 2004.

[45] S. P. Poplack, T. D. Tosteson, W. Wells, B. W. Pogue, P. M. Meaney, A. Hartov, C. A. Kogel, S. K Soho, J. J. Gibson, K. D. Paulsen, “Electromagnetic breast imaging: pilot results in women with abnormal mammography,” Radiology, vol. 243, pp. 350-359, 2007.

[46] M. Miyakawa, H. Ikarashi, N. Ishii, and M. Bertero, “Visualization of the Breast Tumor by the Integrated Use of CP-MCT and Chirp Pulse Microwave Breast Radar,” 35th European Microwave Conf., vol. 2, pp. 1043–1046, 2005.

[47] Micro-Coax, UT-141-SS, Semi-Rigid Coaxial Cable. Data Sheet, 2008. Available online: http://www.micro-coax.com/pages/products/ProductTypes/CableTypes/Semi-RigidCoaxial/Semi-RigidDetails.asp?ID=UT-141C-SS

[48] OMMIC, CGY2108HV, Dual Ultra Low Noise High IP3 Amplifier. Data Sheet, 2005.

[49] Hittite Microwave Corporation, HMC478MP86 / 478MP86E, SiGe HBT Gain Block MMIC Amplifier, DC - 4.0 GHz, Data Sheet, 2006. Available online: http://www.hittite.com/content/documents/data_sheet/hmc478mp86.pdf.

[50] Mini-Circuits®, Frequency Mixers, Surface Mount, Level 7, 50 kHz to 12 GHz, ADE/ADEX. Data Sheet, 2005. Available online: http://www.minicircuits.com/products/fm_sm_level_7.html.

[51] Analog Devices, Inc., Single-Supply, Rail-to-Rail Low Power FET-Input Op Amp AD822. Data Sheet, 2005. Available online: http://www.analog.com/static/imported-files/Data_Sheets/AD822.pdf.

[52] M/A-COM Inc., MASW-007071-000100, GaAs SPDT Switch, Absorptive, Single Supply, DC-4 GHz, Data Sheet, 2006. Available online: http://www.macom.com/DataSheets/MASW-007071-000100.pdf.

[53] M/A-COM Inc., MASW-007070-000100, GaAs SPST Switch, Absorptive, Single Supply, DC-4 GHz, Data Sheet, 2006. Available online: http://www.macom.com/DataSheets/MASW-007070-000100.pdf.

[54] Agilent, Agilent N5181A MXG and N5161A MXG ATE Analog Signal Generators, Data Sheet, 2008.

[55] F. Di Paolo, Networks and Devices Using Planar Transmission Lines, Boca Raton: CRC Press LLC ,2000.

[56] P. Meaney, K. Paulsen, B. Pogue, and M. Miga, "Microwave Image Reconstruction Utilizing Log-Magnitude and Unwrapped Phase to Improve High-Contrast Object Recovery," IEEE Transactions on Medical Imaging, vol. 20, no. 2, pp. 104–116, 2001.

[57] T. Rubæk, O. S. Kim, and P. Meincke, "Computational Validation of a 3-D Microwave Imaging System for Breast-Cancer Screening," IEEE Transactions on Antennas and Propagation, vol. 57, no. 7, pp. 2105-2115, 2009.

[58] T. Rubæk, P. M. Meaney, P. Meincke, and K. D. Paulsen, "Nonlinear Microwave Imaging for Breast-Cancer Screening using Gauss-Newton's Method and the CGLS Inversion Algorithm," IEEE Transactions on Antennas and Propagation, vol. 55, no. 8, pp. 2320–2331, 2007.

[59] O. S. Kim and P. Meincke, "Adaptive Integral Method for Higher Order Method of Moments," IEEE Transactions on Antennas and Propagation, vol. 56, no. 8, pp. 2298–2305, 2008.

[60] O. S. Kim and P. Meincke, "3-Dimensional Iterative Forward Model for Microwave Imaging," Proc. 4th International Workshop on Biological Effects of Electromagnetic Fields, vol. 1, Hersonissou, Greece, October 2006, pp. 306–310.

[61] P. C. Hansen, Rank-Deficient and Discrete Ill-Posed Problems: Numerical Aspects of Linear Inversion, ser. Monographs on Mathematical Modeling and Computation. SIAM, 1998.